Climate Dynamics
https://doi.org/10.1007/s00382-021-06070-7

The causal role of South China Sea on the Pacific–North American teleconnection pattern

Yinchen Zhang[1] · **X. San Liang**[2,3,4]

Received: 7 June 2021 / Accepted: 18 November 2021

Abstract
The Pacific–North American (PNA) teleconnection pattern is shown to be remarkably influenced by the South China Sea (SCS), through causal inference with information flow, a real physical notion which has just been rigorously derived from first principles. The information flow rate, which measures the strength of causality from the Pacific sea surface temperature anomaly (SSTA) to the PNA index, shows a distinct causal pattern within the SCS. This pattern is rather robust; it exists with different datasets, and lasts through time. To validate, sensitivity experiments have been designed with purported SCS warming and cooling. By comparing the forced PNA evolutions to the standard case, PNA-like responses have been revealed. Specifically, relatively strong positive (negative) SCS SSTA would trigger a positive (negative) propagating PNA-like response. The responding wave train carries energy toward Pacific and North America, and hence affects the PNA growth. Also located is the wave origin using the Rossby wave source diagnosis. This study suggests that the SCS effect should be taken into account in interpreting and predicting PNA.

Keywords South China Sea · Pacific–North American teleconnection pattern · Information flow · Tropical forcing · Sensitivity experiment

1 Introduction

The Pacific–North American (PNA) teleconnection pattern is one of the dominant low-frequency modes of the boreal winter midlatitude atmosphere (Wallace and Gutzler 1981; Barnston and Livezey 1987). It plays a major role in the hydroclimate variability of the North Pacific–American sector (e.g., Leathers et al. 1991; Renshaw et al. 1998; Archambault et al. 2010), including the atmospheric river activity over North America (e.g., Toride and Hakim 2021), and may extend its impact to remote regions (e.g., Pinto et al. 2011; Drouard et al. 2015). Clearly, a better understanding of PNA will benefit intraseasonal climate prediction, which is urgent to be improved (Baxter and Nigam 2013).

The mechanism of PNA growth has been extensively investigated. By the prevailing points of view, it can be generated through (1) linear dispersion of Rossby wave excited by tropical forcing (e.g., Hoskins and Karoly 1981; Jin and Hoskins 1995; Trenberth et al. 1998; Seo et al. 2016), (2) barotropic amplification associated with the zonal asymmetric climatological flow (e.g., Simmons et al. 1983; Branstator 1990, 1992; Li and Wettstein 2012), (3) dynamical feedback from synoptic transient eddies (e.g., Lau 1988; Zhou et al. 2017; Song 2018; Chu et al. 2020). The three are not mutually exclusive (e.g., Cash and Lee 2001; Dai et al. 2017), and the tropical excitation forms a key role. Although PNA as a midlatitude mode could be naturally inherent from the midlatitude atmosphere itself, a specific tropical forcing is still essential for it to grow (Mori and Watanabe 2008). Indeed, the role of external tropical forcing in PNA growth is found to be more important than that in the formations of other teleconnection modes; for example, Feldstein (2000)

✉ X. San Liang
sanliang@courant.nyu.edu

[1] School of Atmospheric Sciences, Nanjing University of Information Science and Technology, Nanjing 210044, China

[2] Department of Atmospheric and Oceanic Sciences, Institute of Atmospheric Sciences, Fudan University, Shanghai 200438, China

[3] IRDR ICoE on Risk Interconnectivity and Governance on Weather/Climate Extremes Impact and Public Health, Fudan University, Shanghai 200438, China

[4] Shanghai Qi Zhi Institute (Andrew C. Yao Institute), Shanghai 200232, China

Published online: 26 November 2021

suggested that the signal-to-noise ratio (external forcing vs. internal stochastic process) for PNA is 1.11, while that for the North Atlantic Oscillation (NAO) is only 0.09. The tropical forcing is also found to be of importance in determining the PNA life cycle (Franzke et al. 2011; Branstator 2014), which is about 2–3 weeks and is dominated by linear processes (e.g., Feldstein 2002; Luo et al. 2020).

In the tropics, the dominant interannual mode is El Niño – Southern Oscillation (ENSO). Accordingly, its impact on PNA has long been studied. It is found that PNA tends to be in its positive (negative) phase more frequently during El Niño (La Niña) years. For this reason, in early literature, the mode has been considered as the extratropical response to ENSO forcing in the form Rossby waves (e.g., Horel and Wallace 1981; Simmons 1982). Observations, however, seem to be inconsistent with the connection. For example, no PNA event occurs during the 1972/73 El Niño, whereas in the 1980/81 winter, there is an obvious PNA but no ENSO occurs. Even reversed correlation exists, e.g., a prolonged positive PNA event encounters the 1984/85 La Niña. These indicate that ENSO cannot fully explain PNA, as suggested in previous works (e.g., Renshaw et al. 1998; Straus and Shukla 2002), and reportedly it accounts for only about 29% of the PNA variance (Li et al. 2019). The remainder variance, apart from internal dynamics, has been explained by other external tropical forcings such as Madden–Julian Oscillation (MJO), to which a phase locking has been accredited (e.g., Mori and Watanabe 2008; Riddle et al. 2013) and optimal initial conditions of PNA growth have been studied (e.g., Henderson et al. 2020), but much is yet to be explored. For the exploration of external forcings, many efforts have been made, including the slow feature analysis (e.g., Yang et al. 2016; Zhang et al. 2017a, b), and the key to exploration is the revelation of causality.

In this study, we employ a newly developed rigorous and quantitative causality analysis to investigate other possible tropical forcing(s) that may drive or impact PNA. Our domain of interest is Pacific, the largest oceanic division and the dominant source of tropical forcing. As will be seen soon, our causal inference confirms the previous discoveries but, surprisingly, also reveals a strong causal influence from the South China Sea (SCS).

We will henceforth investigate how SCS impacts PNA. In the following we first introduce the rigorously developed tool of causal inference, namely, the Liang-Kleeman information flow analysis. In Sect. 3, the causality analysis results are presented. These results are then verified through numerical model simulations (Sect. 4). In Sect. 5, a dynamical interpretation is supplied, and Sect. 6 summarizes the study.

2 Liang–Kleeman information flow

We will be using the information flow-based causality analysis (Liang, 2014) to fulfill the objective of this study. Information flow (IF) is a fundamental and widely-applied concept in general physics, but it had not been rigorously formulated until the recent studies initialized by Liang and Kleeman (2005); see Liang (2016a) for a rigorous formalism with respect to arbitrary dynamical systems. An important application is causality analysis, a milestone being the time series causal inference by Liang (2014), which we hereafter give a brief review of the part pertaining to this study. Consider a dynamical system

$$\frac{d\mathbf{x}}{dt} = \mathbf{F}(\mathbf{x}, t) + \mathbf{B}(\mathbf{x}, t)\dot{\mathbf{w}}, \tag{1}$$

where $\mathbf{x}$ and $\mathbf{F}$ are n-dimensional vectors, $\mathbf{B} = (b_{ij})$ is an $n \times m$ diffusion coefficient matrix, $\mathbf{w}$ is an m-vector of standard Wiener process ($\dot{\mathbf{w}}$ is the so-called white noise). $\mathbf{F}$ and $\mathbf{B}$ are assumed to be differentiable. Liang (2008) proved that, when $n = 2$, the IF rate (unit: nats per unit time) from X_2 (the random variable corresponding to x_2) to X_1 is

$$T_{2\to 1} = -E\left[\frac{1}{\rho_1}\frac{\partial(F_1\rho_1)}{\partial x_1}\right] + \frac{1}{2}E\left[\frac{1}{\rho_1}\frac{\partial^2\left(b_{11}^2 + b_{12}^2\right)\rho_1}{\partial x_1^2}\right], \tag{2}$$

where E is mathematical expectation, and ρ_1 the marginal probability density of X_1. Note that the IF rate is asymmetric, i.e., generally $T_{2\to 1} \neq T_{1\to 2}$, distinctly from correlation.

In real problems, we often have time series but the dynamics underlying the system is unknown. In this case, (2) is estimated using maximum likelihood estimation (MLE). Given two time series X_1 and X_2, the MLE of $T_{2\to 1}$ is, by Liang (2014),

$$\widehat{T}_{2\to 1} = \frac{C_{11}C_{12}C_{2,d1} - C_{12}^2 C_{1,d1}}{C_{11}^2 C_{22} - C_{11}C_{12}^2}, \tag{3}$$

where C_{ij} is the sample covariance between X_1 and X_2, and $C_{i,dj}$ is that between X_i and a Euler forward differenced series derived from X_j, i.e., $\dot{X}_{j,n} = \left(X_{j,n+k} - X_{j,n}\right)/(k\Delta t)$, with $k \geq 1$ some integer, Δt the time step. Note that Euler forward difference is somewhat irreplaceable despite its lower accuracy, because of a common sense that present could affect future but not vice versa.

A nonzero $T_{2\to 1}$ indicates that X_2 causes X_1. Conversely, X_2 is not causal if $T_{2\to 1} = 0$, consistent with the principle of nil causality (Liang 2016a), a proven theorem in the IF theory while other empirical formalisms attempt to verify in applications. It can be seen in Eq. (3) that if $C_{12} = 0$, then $\widehat{T}_{2\to 1} = 0$, but not vice versa. Hence a corollary is that, "in the linear sense, causation implies correlation, but

correlation does not imply causation" (Liang 2014). This corollary still holds even in the extreme situation when the total information vanishes (Liang and Yang 2021). In an explicit way this ends the long-standing debate on causation vs. correlation.

The above theory and causal inference method have been successfully applied to many real problems. Recently, Jiang et al. (2019) used it to investigate the individual influences of the land cover, sea temperature, sea ice and carbon dioxide concentration on the global climate. They found that, in winter, all these tend to produce a positive-phase PNA pattern, which makes the North American colder. The changes of CO_2 and sea ice lead to a negative NAO phase, and hence induce cold winters over Europe, just as observed in 2018. In other studies, Tao et al. (2021) used Liang–Kleeman information flow to quantify the relative contributions of global warming, Atlantic Multidecadal Oscillation (AMO) and Interdecadal Pacific Oscillation (IPO) to the land precipitation variabilities since 1930s; Xiao et al. (2020) identified a one-way causality from the driving forces to Arctic mean temperature anomaly (AMTA), and found that, during the first warming stage (1920–1938), the Pacific Decadal Oscillation (PDO) and aerosols are the main factors determining the change in AMTA, and during the second warming stage (1977–2018), greenhouse gases (dominated by CO_2) are the major factors accounting for the Arctic warming.

3 Causal inference with the Liang–Kleeman information flow analysis

We are now applying the information flow analysis to infer the causality from the Pacific sea surface temperature (SST) variability to the PNA variability. The former is represented by the monthly SST anomaly (SSTA) derived from Hadley Centre Sea Ice and Sea Surface Temperature (HadISST; Rayner et al. 2003) dataset with a horizontal resolution of 1° by 1°; the latter is the monthly PNA index (PI) from the NOAA Climate Prediction Center (CPC; https://www.cpc.ncep.noaa.gov/data/teledoc/teleindcalc.shtml). The period from 1981 to 2010 is selected, considering the 1976/77 climate shift of the Pacific (e.g., Miller et al. 1994) and the improvement of data quality control since the 1980s. The monthly anomaly is obtained by subtracting the 1981 −2010 monthly climatology from the total field.

On each grid point, the time series of the SSTA and the PI are respectively assigned to X_2 and X_1, and the IF rate (indicating causality) from X_2 to X_1 (denoted as $\widehat{T}_{2\to1}$) is calculated according to Eq. (3). Ideally if $\widehat{T}_{2\to1} \neq 0$, then X_2 is causal to X_1 and $\left|\widehat{T}_{2\to1}\right|$ measures the strength of the causality (see Liang 2014). In practice, of course a significance test must be performed. The spatial distribution of $\widehat{T}_{2\to1}$ is shown in Fig. 1, and those significant at the 95% confidence level are marked with slashes. As can be seen, there is a large area of high causality in the central and eastern equatorial Pacific, which is reminiscent of the canonical ENSO pattern. This tells the role of ENSO in the PNA formation, a fact that has been well established: substantial ENSO-related SSTA can arouse deep convective source, which then produces a Rossby wave response propagating to the extratropics (e.g., Shukla and Wallace 1983; Trenberth et al. 1998). Our causality analysis has recovered this well-established fact.

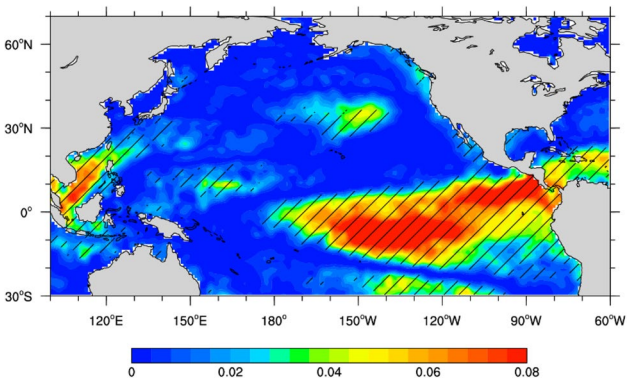

Fig. 1 Spatial distribution of the IF rate $\widehat{T}_{2\to1}$ (in nats/month) from the Pacific SSTA to the PNA index for the period of 1981 −2010. Slashed areas indicate values that exceed 95% confidence level

Apart from the impact from ENSO, a surprisingly high center of causality is clearly seen in Fig. 1 within the South China Sea (SCS), the largest semi-closed marginal sea in the western Pacific (WP). It is observed that SCS has a surface warm pool over 28 °C during most of the year (e.g., Liu et al. 2002; Li et al. 2007), which can influence the tropical cyclone genesis, Asian monsoon, precipitation, etc. (e.g., Wang et al. 2007; Roxy and Tanimoto 2012; Vaid and Polito 2016), and may extend the influence to the extratropics. In this case, the causality from SCS indeed reaches the extratropics, as shown in the distribution of the IF rates from the SCS regional mean (3.5°–21.5°N, 104.5°–118.5°E) SSTA to the 250- and 500-hPa geopotential height anomalies [derived from the NCEP Climate Forecast System Reanalysis (CFSR; Saha et al. 2010)] (Fig. 2). Specifically, the two high-latitude centers of the causality pattern closely resemble two of the PNA centers, both for the middle and upper troposphere, in accordance with the equivalent barotropic structure of PNA. Compared with the middle troposphere (Fig. 2b), in the upper troposphere, there is a noticeable trace of centers in the tropics and subtropics (Fig. 2a), which may provide a clue to the response process. The large causality occupying the tropics and subtropics may reflect the intrinsic processes, e.g., equatorial Kelvin waves, that may carry the effect of SCS SST eastward. This, however, is beyond the scope of this study.

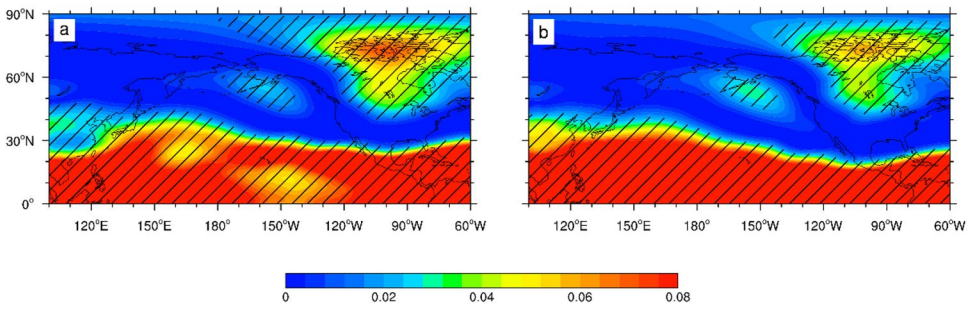

Fig. 2 As in Fig. 1, but for the IF rates from the SCS regional mean SSTA to the **a** 250- and **b** 500-hPa geopotential height anomalies

Notably, the high causality pattern over the SCS appears quite localized and concentrated in the interior of the SCS (Fig. 1) rather than its periphery, including the Luzon Strait (LS), the major SCS-Pacific passage. Through the Strait, the Kuroshio carrying the WP water has been reported to continually intrude into the SCS, and affect its thermal and dynamic properties (e.g., Nan et al. 2015; Zhao et al. 2016). The LS is also the major inflow channel of the SCS throughflow, a conveyor of heat and freshwater (e.g., Qu et al. 2006; Gordon et al. 2012). Herein, however, the IF rate over the LS appears much weaker, from another aspect demonstrating that the causality is not from the WP, but from the SCS local variability. The weak causality over the LS should be due to the water exchange with the interior SCS through the outflow as observed in, say, Nan et al. (2015).

The SCS SST-to-PNA causality is rather robust. For each of three decades of 1981–2010, the IF rates are calculated and shown in Fig. 3a–c. As can be seen there always exists a causal center within the SCS, plus the strong ENSO-related pattern. In addition, both causal patterns appear most intense during the 1991–2000 period, and the former is weaker during 1981–1990 while the latter is weaker and more biased to the central Pacific during 2001–2010. Despite the decadal variability, such causalities always exist. Moreover, it implies a unique decadal variability of the causality from SCS, which is different from that related to ENSO. In general, the revealed causalities stay robust regardless of the varying time domain. We have tried another dataset, namely, the CMCC Global Ocean Reanalysis System version 5 (C-GLORSv5; Storto and Masina 2016), essentially similar results are obtained; shown in Fig. 3d is an example, where the causality patterns during the 1981–2010 resemble those in Fig. 1, though appearing slightly weaker.

It should be mentioned that there is also strong causal center in the midlatitude North Pacific center of PNA (Figs. 1 and 3a, c, d). We will explore this in the future. In the following we focus on the role of SCS to PNA.

Admittedly, the SCS can be influenced by ENSO (e.g., Wang et al. 2006; Yang et al. 2015). Such complex relationships among PNA, SCS and ENSO may account for the long ignorance of the SCS role in the formation of PNA. Nonetheless, these intricate relationships can be unraveled using a generalized multivariate causality analysis just developed (Liang 2021). Consider a d-dimensional stochastic dynamical system, by derivation the maximum likelihood estimator of the IF rate from X_j to X_i, under a linear assumption, is

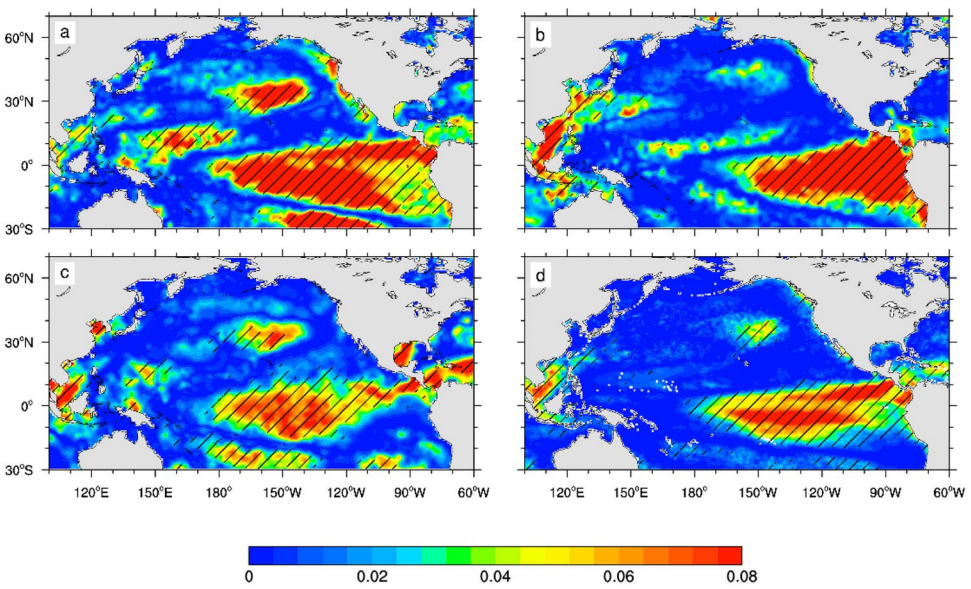

Fig. 3 As in Fig. 1, but for the period of **a** 1981 – 1990, **b** 1991 –2000, and **c** 2001 –2010. **d** For the period of 1981 –2010 but based on the C-GLORSv5 dataset

$$\widehat{T}_{j\to i} = \frac{1}{\det \mathbf{C}} \bullet \sum_{k=1}^{d} \Delta_{jk} C_{k,di} \bullet \frac{C_{ij}}{C_{ii}}, \tag{4}$$

where C_{ij} and $C_{i,dj}$ are as those in Eq. (3), Δ_{ij} the cofactors of the matrix $\mathbf{C} = (C_{ij})$, and $\det \mathbf{C}$ means the determinant of $\mathbf{C}$. When $d = 2$, it is easy to show that this is reduced to Eq. (3). It is capable of revealing the direct causality between two certain components within the multivariate system. Application of this to the time series of the PNA index, the regional mean SSTA of SCS, and Niño 3.4, the direct IF rate from SCS SSTA to PNA is 0.0584, exceeding the 95% confidence level (0.0260). Such robust causality indicates that the SCS indeed exerts its own impact on PNA.

4 Model verification of the causal inference

4.1 Model and data

We now check with the Community Earth System Model (CESM) version 1.2.2 (Hurrell et al. 2013), a widely-used global climate model developed by NCAR, whether the above-revealed causality is correct, and what it implies. For all simulations we adopt the F1850PDC5 component set, which includes the Community Atmosphere Model version 5 (CAM5; Neale et al. 2010) and the Community Land Model version 4 (CLM4; Oleson et al. 2010); its ocean and ice components are prescribed in the form of a surface boundary forcing dataset, i.e., a merged product based on the monthly HadISST1 and NOAA OI SST analysis (Hurrell et al. 2008). This component set is not fully atmosphere–ocean coupled; nonetheless, it is capable of detecting atmospheric responses to the ocean surface variations (Hurrell et al. 2008), which is the primary concern of this study. The adopted grid type is f09_g16 (horizontal resolution of about 1°) and there are 30 hybrid sigma/pressure levels in vertical.

The CFSR dataset (cf. Sect. 3) is used to form the reference state. The variables include daily averaged geopotential height, zonal and meridional winds, and temperature. The horizontal resolution is 0.5° and the time range covers the extended boreal winters (November–March) from 1980/81 to 2009/10 (30 winters). The daily data from NOAA Optimum Interpolation (OI) SST version 2 (Reynolds et al. 2007) and the Oceanic Niño Index (ONI; https://origin.cpc.ncep.noaa.gov/products/analysis_monitoring/ensostuff/ONI_v5.php) are also utilized.

4.2 Simulation of PNA (control run)

First, we make a control run (CTL), with a daily output from 1970 to 2010 (41 years, the first 10 years discarded for spin-up). The CTL results are compared to the reanalysis (CFSR) result with respect to the spatial pattern and space–time evolution of PNA. Similar to Mori and Watanabe (2008), the PNA pattern is identified by applying a rotated empirical orthogonal function (REOF) analysis to the 10-day low-pass filtered daily anomaly of the 500-hPa geopotential height over the North Pacific sector (0°–90°N, 120°E–60°W) for the aforementioned 30 winters. Specifically, the patterns for CFSR and CTL data are, respectively, obtained as the first REOF modes by rotating 5 leading modes following the varimax criterion (e.g., Barnston and Livezey 1987; Lian and Chen 2012). The results are shown in Fig. 4. Clearly, the typical quadrupole pattern of PNA has been well captured in the simulation (Fig. 4b), similar to the reanalysis counterpart (Fig. 4a).

The time series corresponding to the two modes are normalized as the PIs. A positive (negative) PNA event is identified when the PI is above 1.2 (below − 1.2) and lasts at least 5 days, and the peak day is called day 0. For each event, 21 days from day − 10 to day + 10 are analyzed, which makes a life cycle. Those events far from monotonic growth and decay are discarded. In doing this, 36 positive and 36 negative PNA events for the CTL dataset are identified, so are for the CFSR dataset. The 21-day composited PIs for both phases are shown in Fig. 5. It shows that the PI variations for the CTL (Fig. 5b) and the CFSR (Fig. 5a) datasets are quite similar. Note that the negative PI amplitude is slightly larger than the positive one, consistent with previous observations and suggestions (e.g., Palmer 1988; Corti and Palmer 1997; Dai et al. 2017; Luo et al. 2020).

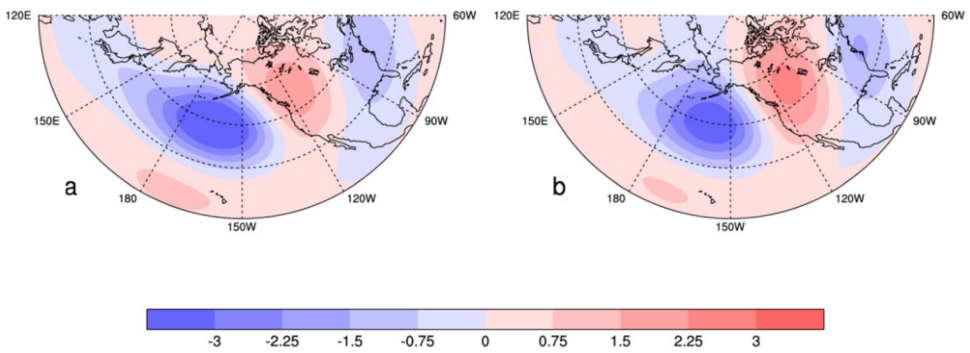

Fig. 4 PNA patterns for **a** CFSR and **b** CTL as the first REOFs, respectively explaining 14.4% and 17.7% of the total variance. The amplitude is normalized and conformed to the positive phase, with the interval of 0.75

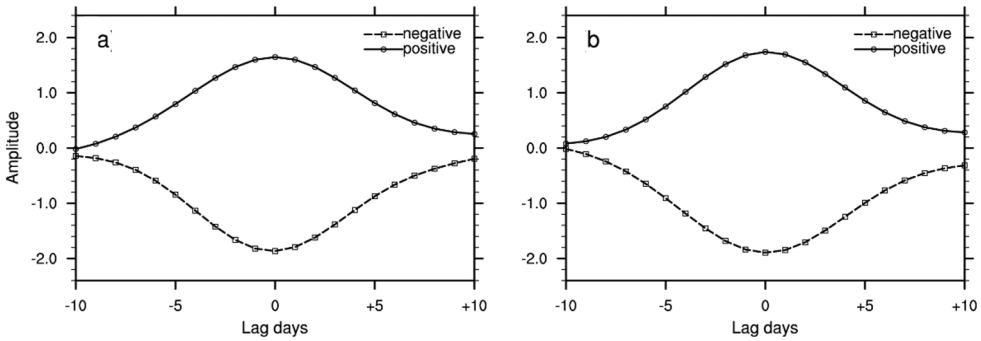

Fig. 5 Composited PNA indices of identified events for **a** CFSR and **b** CTL. Solid lines with circles (dashed lines with squares) represent the positive (negative) phase

The PNA evolution is described by the 250-hPa anomalous quasi-geostrophic stream function (ψ') and the wave activity flux (WAF; Takaya and Nakamura 2001). The quasi-geostrophic stream function is defined as $\psi = \Phi/f$, where Φ is the geopotential and f the Coriolis parameter, and the anomaly ψ' is the deviation from climatology for a certain time domain. The horizontal expression of the WAF can be simply written as

$$\mathrm{WAF} = \frac{1}{2|\mathbf{U}|}\begin{pmatrix} U\left(\psi_x'^2 - \psi'\psi'_{xx}\right) + V\left(\psi'_x\psi'_y - \psi'\psi'_{xy}\right) \\ U\left(\psi'_x\psi'_y - \psi'\psi'_{xy}\right) + V\left(\psi_y'^2 - \psi'\psi'_{yy}\right) \end{pmatrix}, \tag{5}$$

where subscripts denote partial derivatives, and $\mathbf{U} = (U, V)$ the climatological flow. For detailed formalism, see Takaya and Nakamura (2001). A chain of ψ' with alternate signs represents the wave train, and the associated WAF indicates the direction of the wave energy propagation. Such fields are composited for each phase. Figure 6 presents the positive-phase pre-peak composites with, respectively, the CFSR (left column) and the CTL (right column) datasets. Figure 7 shows the negative counterparts. The simulated composites show a steady typical growth of PNA, which resemble its reanalysis counterpart, except for slightly larger amplitude of high-latitude ψ'. By day −4, a rapid growth of both ψ' and WAF occurs, which may be due to the Asian westerly jet exit, where has been identified as a key region with barotropic amplification (e.g., Simmons et al. 1983; Mori and Watanabe 2008). The wave dispersion is also seen.

The CTL results illustrate the climatological features of PNA. The close resemblance to their reanalysis counterparts indicates that the model is successful in reproducing the PNA dynamics. Moreover, the SCS-to-PNA causality has also been recovered successfully in the simulation. The estimated IF rate (for 1981–2010) from the input SCS mean SSTA to the model output-based PI is 0.0236, exceeding the 95% confidence level (0.0150).

4.3 Verification

In this section the direct SCS-to-PNA causality will be verified through numerical experiments. What we want to demonstrate is that PNA events can occur during periods without ENSO events but with favorable conditions of SCS SST. Hereafter the PNA events most relevant to the SCS are composited. Among the identified events for the control run, the cases are selected for those occurring during non-ENSO periods and when the SCS is active, with its relatively large SSTA positively correlated with the phase of PNA. According to the criteria, 8 negative and 4 positive events are screened out. Such SCS-related PNA evolutions are composited for each phase, also described by the 250-hPa ψ' and WAF (Figs. 8 and 9). As can be seen in the evolution of negative-phase PNA (Fig. 8), by day −9, a cyclonic center (marked in the figure as Center 1) appears over the Yellow Sea and the Sea of Japan, just near the core of the Asian jet. Afterwards, Center 1 grows and propagates downstream, undulating along the jet axis, before an anticyclonic center (marked as Center 2) appears upstream, which is detected in the overall negative-phase composites (Fig. 7). By day −4, Center 1 reaches the aforesaid crucial jet exit region, and the wave train and associated WAF amplify and disperse into the northern and southern branches. The northern branch emanates along a great circle route toward North America, and the southern branch turns southeastward to the subtropics. Then Center 1 tends to merge with the subtropical Pacific center. It indicates that the wave energy propagates to the PNA region and is transferred to the pre-existing PNA embryo. As it approaches day 0, the PNA pattern matures.

The positive-phase PNA evolution generally resembles to the negative phase, except for an opposite sign (Fig. 9). But the anticyclonic Center 1 and the southern branch appear weaker, probably due to the weak warm state of the SCS. Actually, the SCS rarely becomes very warm in winter, and this could explain the relatively less positive events. Nevertheless, the evolution feature is clearly seen.

The composited SCS-related PNA has a weak vertical structure, generally the evolutions are similar for upper,

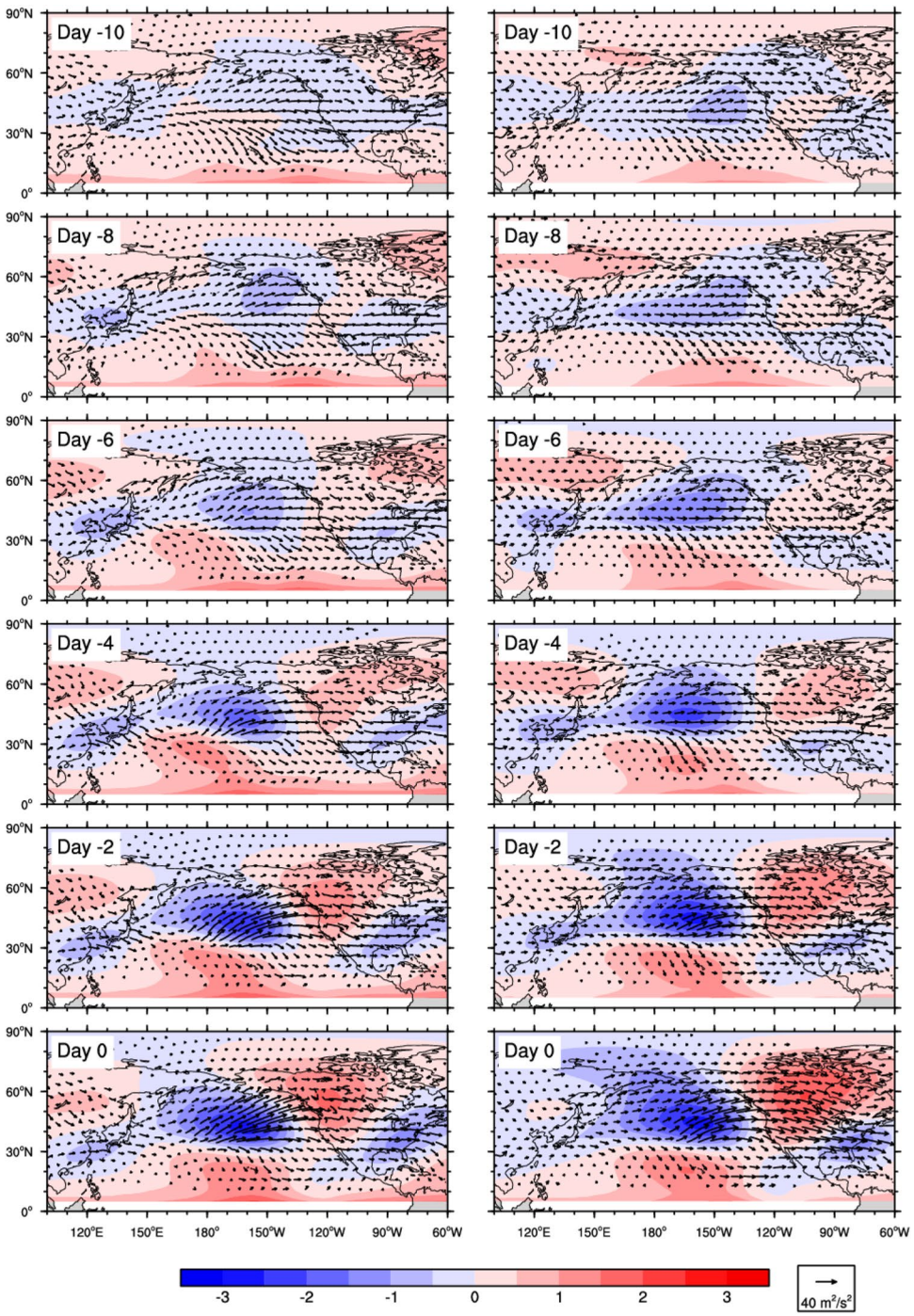

Fig. 6 Composited positive PNA evolution for (left) CFSR and (right) CTL from day − 10 to day 0 with an interval of 2 days, described by the 250-hPa ψ' (shading) and WAF (arrows). Considering the quasi-geostrophic approximation, the fields are calculated poleward of 5°N. The contour interval is 0.5×10^7 m^2 s^{-1} and the arrow scaling is 40 m^2 s^{-2}

middle, and lower troposphere (not shown), consistent with the equivalent barotropic nature of PNA.

Note that the composite SCS-related PNA evolution feature is somewhat different from that of the overall composite (Fig. 8 vs. Fig. 7, Fig. 9 vs. Fig. 6). Especially, the precursory Center 1 in the former is absent in the latter. Center 2 seems to always exist, whatever the causes are, which is also seen in the previous works (e.g., Mori and Watanabe 2008; Baxter and Nigam 2013). Based on these observations, Center 1 may be a reflection of the causality from SCS to PNA, a signal lost in taking the averaging.

To see more clearly how SCS may affect PNA, we conduct sensitivity experiments with respect to certain cases of PNA event. The experiments are listed in Table 1. Among the identified SCS-related events, we select two representative cases, Pos-89 and Neg-90, i.e. a positive event peaking on 12/21/1989, and a negative PNA event peaking on 02/15/1990, respectively. Both cases occur in a non-ENSO

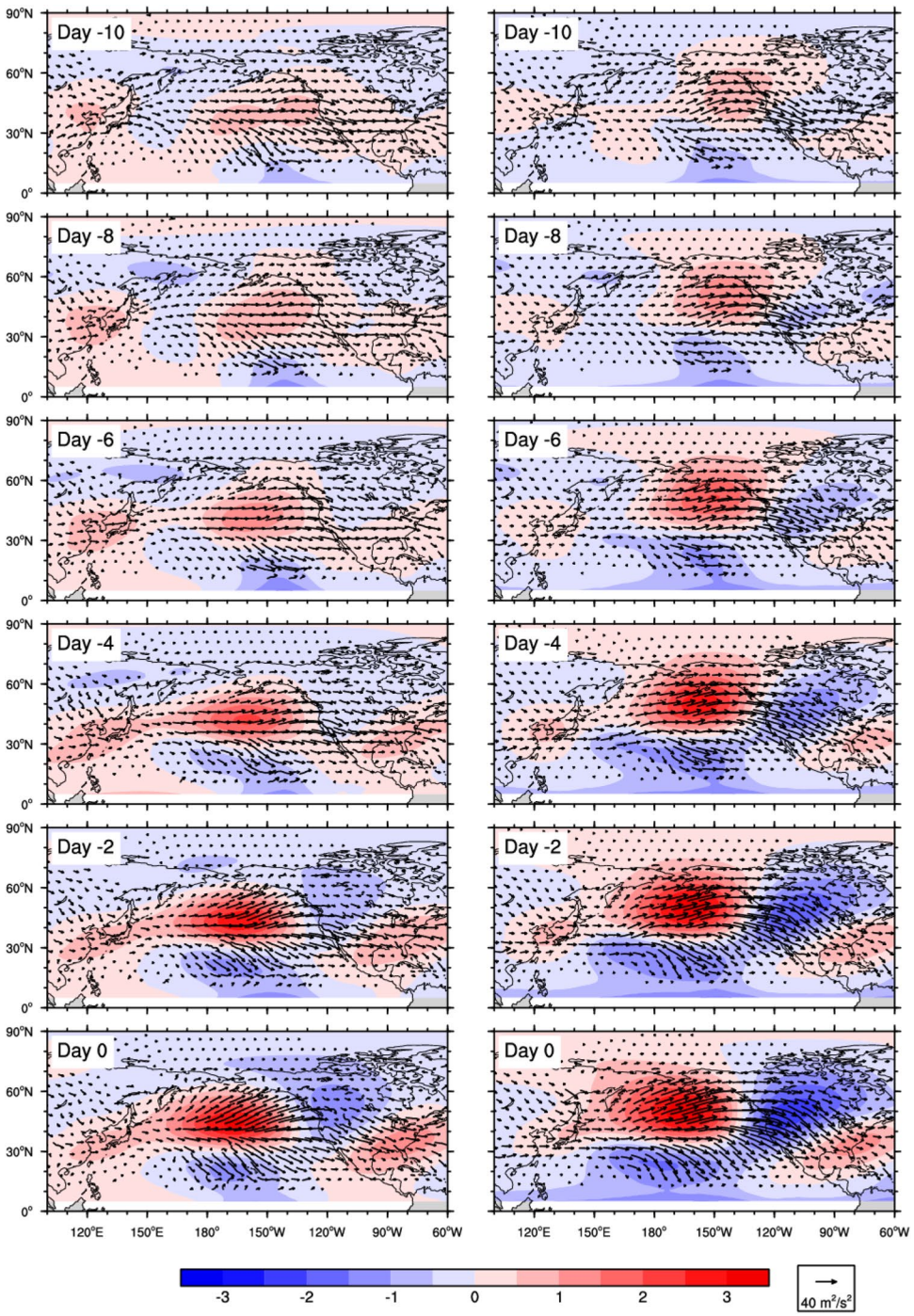

Fig. 7 As in Fig. 6, but for the negative phase

winter. The model input SCS SSTA (based on the climatology) of January 1990, preceding the Neg-90 case, is −2.39 °C, such that a negative PNA event coincides with a cold state of SCS, reflecting the observed correlation. For the Pos-89 case, the SSTA is 0.65 °C in the November 1989 SCS, corresponding to a weak warm state of SCS.

The sensitivity experiments are designed by modifying the SSTs over the SCS region for the 1989/90 winter corresponding to the above cases. Ideally the modification would be done by considering both the specific conditions of SCS SSTA for the cases and the natural annual amplitude of SCS SSTA (about −2 to 2 °C). For the Neg-90

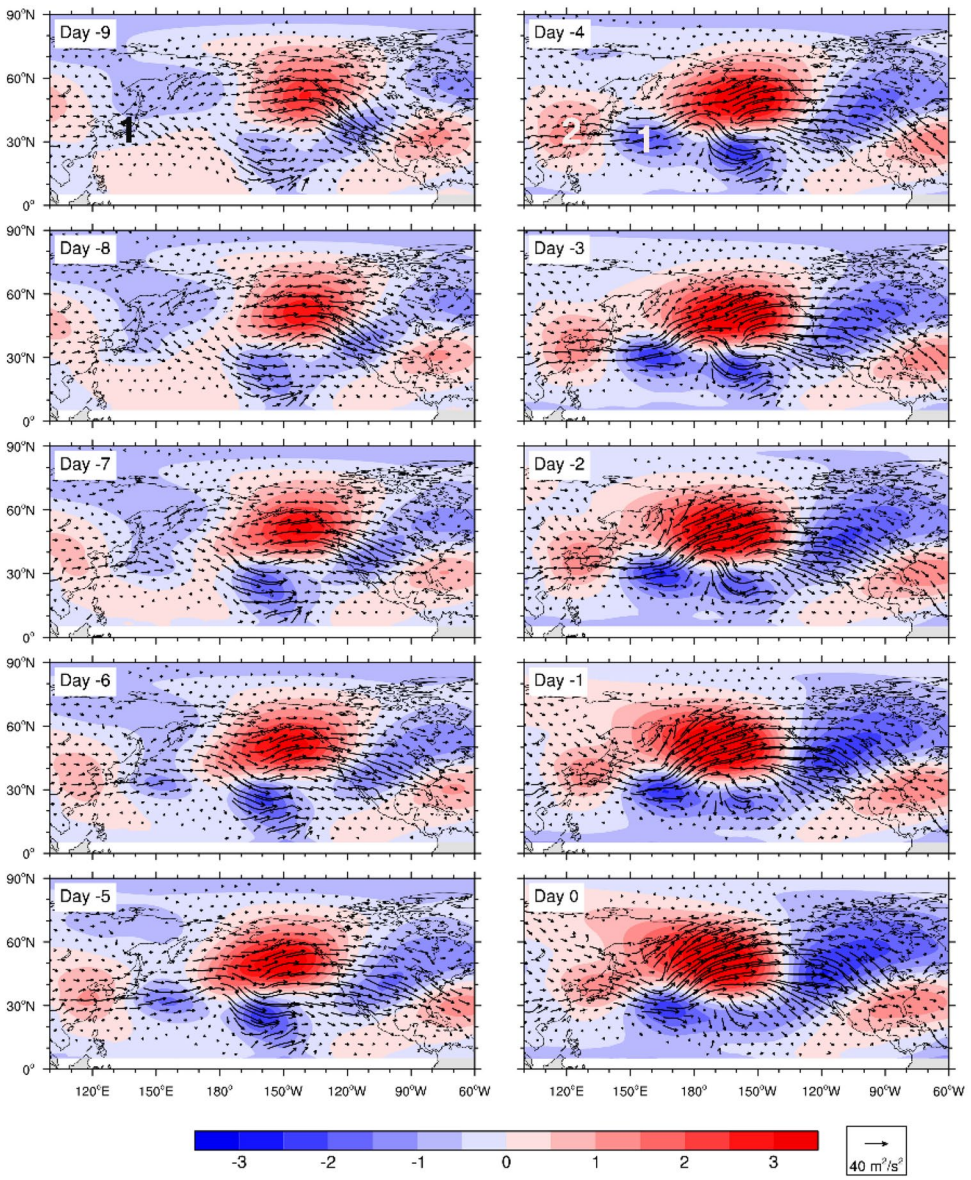

Fig. 8 As in Fig. 6, but for the composited SCS-related negative-phase PNA evolution from day − 9 to day 0. Centers 1 and 2 are marked in white or black

case, we raise the SST by 4 °C everywhere over SCS (the experiment is denoted as SE-P4), turning the cold SCS state to a warm one. For the Pos-89 case, the SCS SST is reduced by 3 °C (denoted as SE-M3), leading to an artificial cold SCS state. More are referred to Table 1.

Originally, the negative-phase PNA evolution for the individual Neg-90 case (Fig. 10) resembles the composited one (Fig. 8), so it is indeed representative. In order to see the response, the difference fields between the results of sensitivity experiment and CTL are examined. The response to the warming of SE-P4 described by the difference fields (SE-P4 minus Neg-90) is presented in Fig. 11. It is closely similar to the original results of Neg-90 in terms of propagation, amplification and dispersion, except for an opposite sign. Interestingly, the key centers in the PNA evolution are in accord with the trace in Fig. 2a. That is to say, the causality inference result actually provides a clue to the response process. Note that the opposite-sign response is approximately twice the amplitude of the original Neg-90 case (Fig. 10) (see the double-scaled color bar), so the imposed SCS warming does change the negative PNA event to a positive PNA-like circulation (not shown). This phase reversal corresponds to the quasi-symmetric cold-to-warm reversal of SSTA (approximately −2 °C to 2 °C), implying a quasi-linear system lies behind.

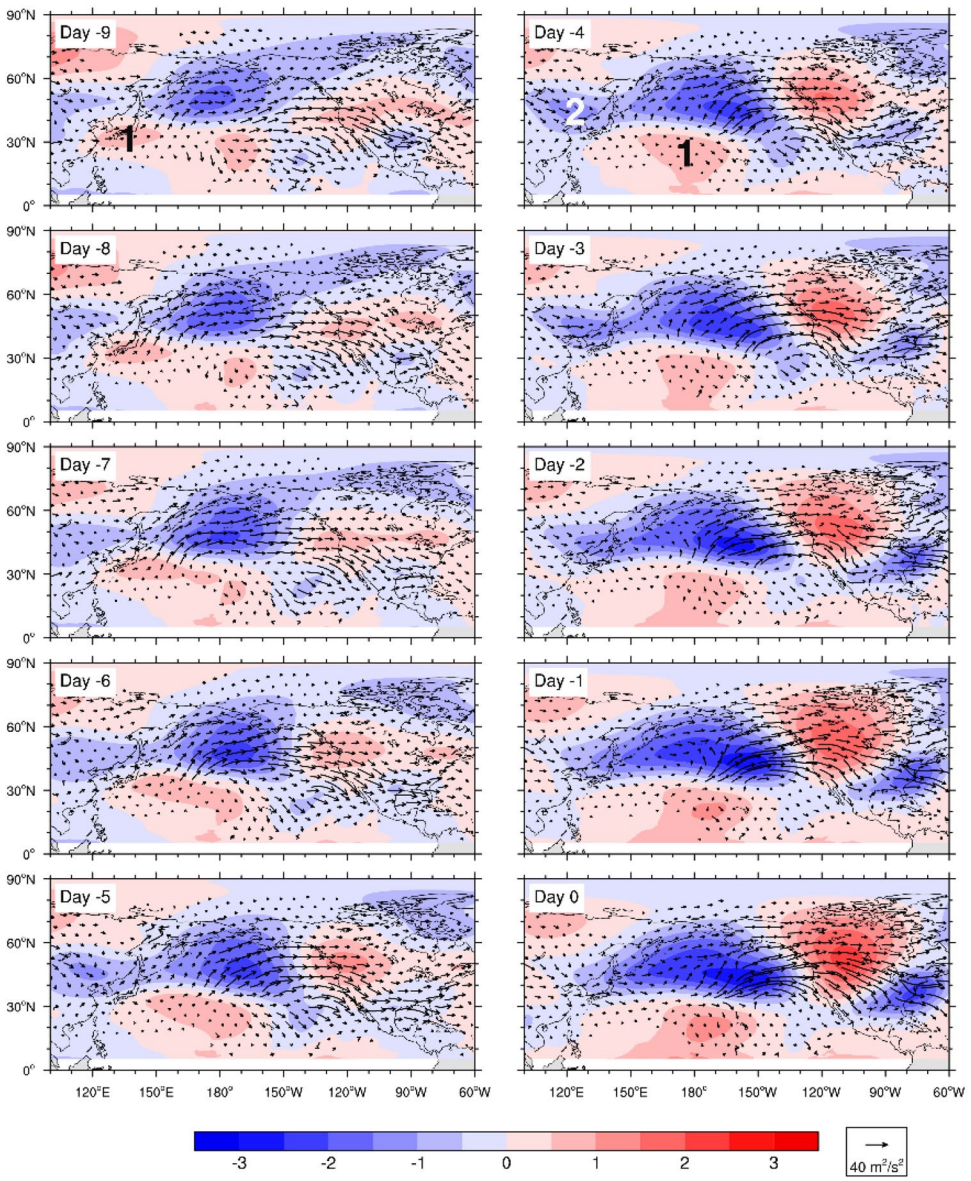

Fig. 9 As in Fig. 8, but for the positive phase

Table 1 Experiments

Experiments	Period of simulation	Runs	Description
Control run (CTL)	1970–2010 (1st decade for spin-up)	Neg-90	Negative PNA around 02/15/1990 Cold SCS
		Pos-89	Positive PNA around 12/21/1989 Weak warm SCS
Sensitivity experiments	1989 – 1991 (initialized with the control run result, with artificial change of SST over SCS)	SE-P4	Raise the SCS SST by 4 °C for the 1989/90 winter with respect to the Neg-90 case, turning a cold SCS state to a warm state
		SE-M3	Reduce the SCS SST by 3 °C for the 1989/90 winter with respect to the Pos-89 case, turning the weak warm SCS state to a cold state

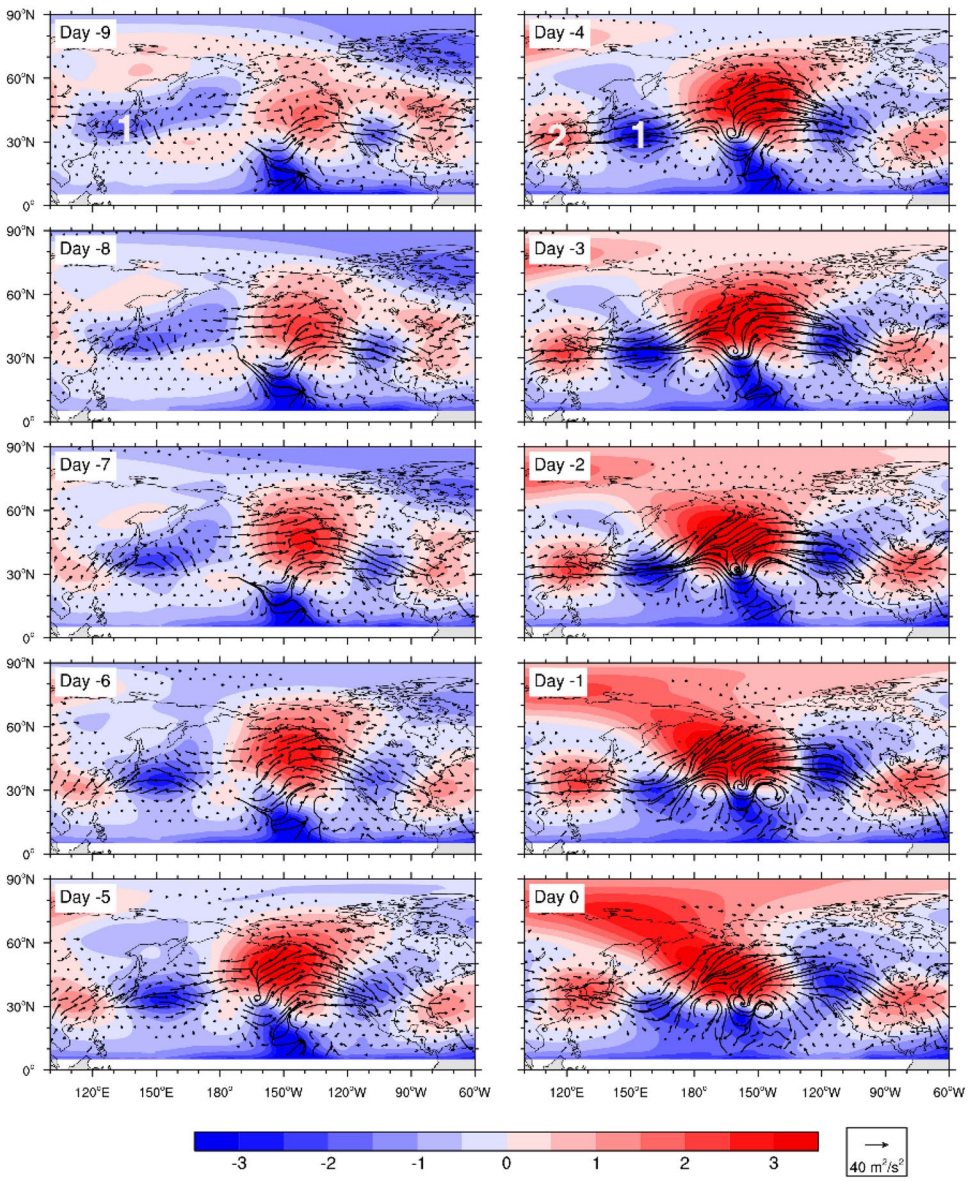

Fig. 10 As in Fig. 8, but for the PNA evolution for the Neg-90 case

Likewise, we have conducted a cooling experiment. The original PNA evolution for the Pos-89 case (Fig. 12) also resembles the composited one (Fig. 9), including the weaker Center 1 due to the weak warm state of SCS. When a cooling applies (SE-M3), the role of SCS is obviously seen. Negative PNA-like response appears in higher amplitudes (Fig. 13), and the positive PNA event is also reversed (not shown). Note that the duration of the response is longer, i.e., the onset is no later than day − 14, especially for the cooling experiment (see Fig. 13).

The results above have revealed a noticeable wave-propagative response aroused by the SCS SSTA, which strongly influences the PNA growth. What leads the response is the precursory Center 1, appearing anticyclonic (cyclonic) for the positive (negative) phase. As a unique feature, Center 1 may indicate the SCS effect. To figure out how the SCS triggers Center 1 and then the entire response, we next focus on the underlying dynamics.

We have also done experiments with other warming/cooling, and the response features are generally similar as long as the SCS SSTA is sufficiently large (not shown).

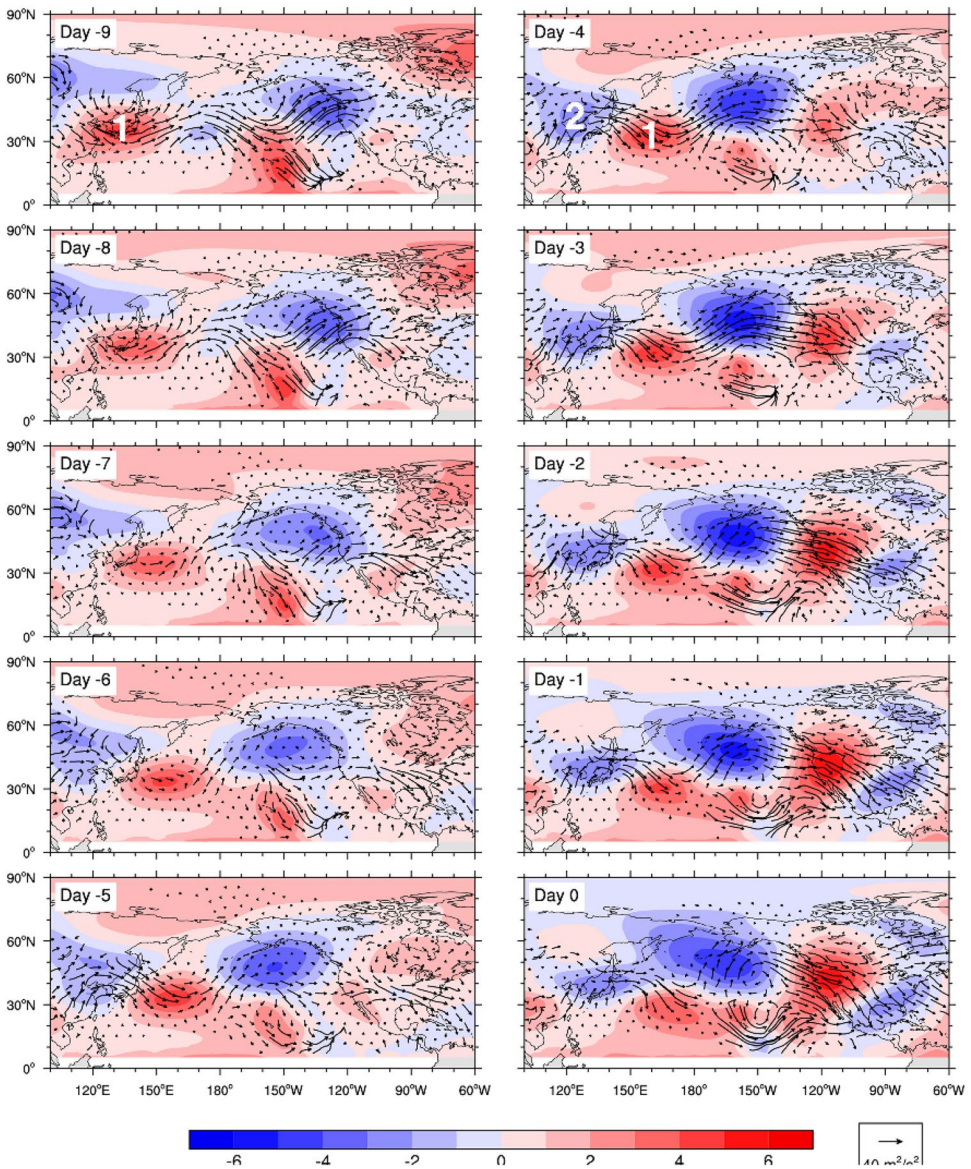

Fig. 11 The evolution of the response to the warming of SE-P4 from day − 9 to day 0. The denotation is the same as Fig. 10 except that the ψ' is for the SE-minus-CTL difference and the WAF is for the SE, and the color bar is double-scaled

5 Dynamical diagnosis

To investigate the underlying dynamics of the SCS SSTA in exciting the PNA pattern, in this section we follow Sardeshmukh and Hoskins (1988) to conduct a diagnosis of its Rossby wave source, which has shown to be suitable for identifying the wave train origin. The barotropic vorticity equation without friction can be written as

$$\left(\frac{\partial}{\partial t}+\mathbf{v}_{\psi}\bullet\nabla\right)\zeta_a=-\mathbf{v}_{\chi}\bullet\nabla\zeta_a-\zeta_a D, \tag{6}$$

where $\mathbf{v}_{\psi}$ and $\mathbf{v}_{\chi}$ are rotational and divergent components of the horizontal wind, ζ_a the absolute vorticity composed of relative vorticity (ζ) and Coriolis parameter (f), and D the divergence. The right-hand side is the very Rossby wave source, in balance with the left-hand side. After filtering and linearization, the anomalous low-frequency wave source S_L can be written as (Mori and Watanabe 2008)

$$S_L=-\left(\overline{\zeta}+f\right)D_L-\mathbf{v}_{\chi L}\bullet\nabla\left(\overline{\zeta}+f\right)-\zeta_L\overline{D}-\overline{\mathbf{v}_{\chi}}\bullet\nabla\zeta_L, \tag{7}$$

where the overbar denotes the climatology, and the subscript L the low-frequency portion through 10-day low-pass filtering. It can be divided into divergence (terms 1 and 3) and advection (terms 2 and 4) components, where terms 3 and

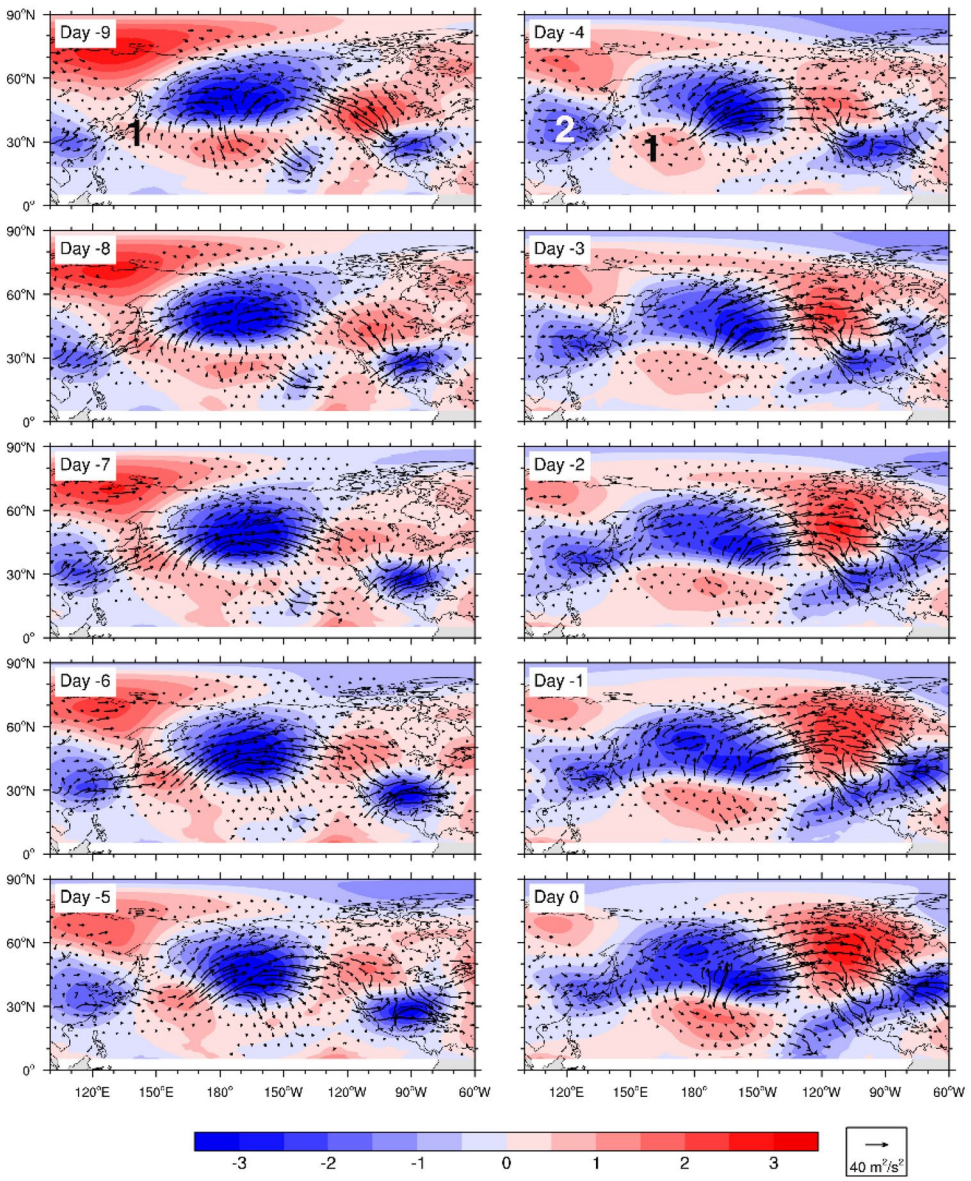

Fig. 12 As in Fig. 9, but for the Pos-89 case

4 are smaller in magnitude and can be omitted. Generally, significant Rossby wave source is closely related to strong tropical forcing (Seo and Lee 2017).

The 250-hPa S_L and its components at the beginning of evolutions are examined. Shown in Fig. 14 are their anomalies for SE-P4 at day − 14. The imposed SCS warming triggers anomalous upper-level divergence that has extended to the north (Fig. 14a), where the Asian westerly jet lies. As is known, strong positive (negative) climatological relative vorticity locates on the north (south) side of the jet axis, hence a positive meridional gradient maximum on the axis, and the absolute vorticity there ascends poleward. The SCS-related divergence coincides with such jet effect (Fig. 14a), and their combined action represented by $-\left(\overline{\zeta}+f\right)D_L$ generates negative pattern of the divergence component of S_L (Fig. 14c). On the other hand, the diverging divergent wind crosses the jet axis (Fig. 14b) and this favors the advection component $-\mathbf{v}_{\chi L}\bullet\nabla\left(\overline{\zeta}+f\right)$ (Fig. 14d), the pattern of which, though, appears weaker for this case. For the total S_L, the superimposed negative pattern prevails (Fig. 14e), and, as a source of negative vorticity (Sardeshmukh and Hoskins

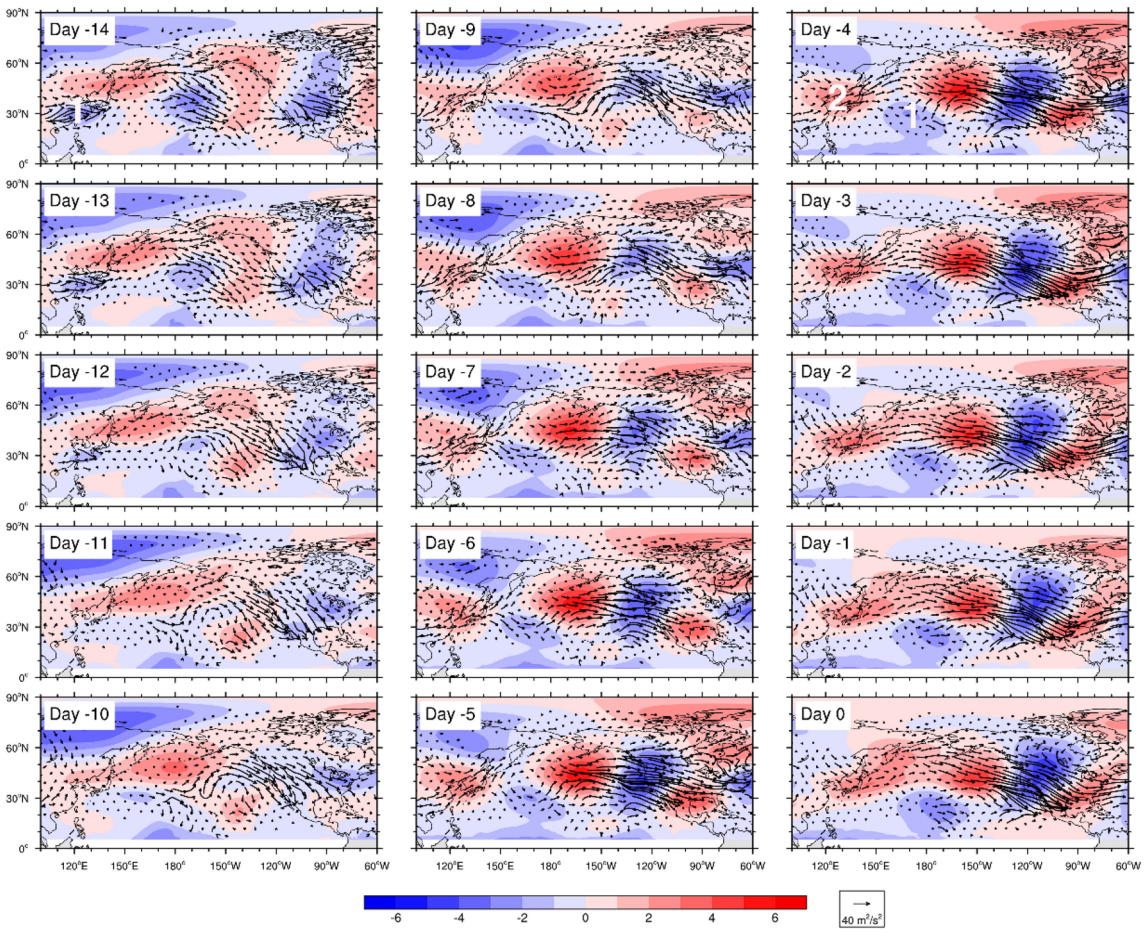

Fig. 13 As in Fig. 11, but for SE-M3, and depicted from day − 14

1988), it induces an initial anticyclonic anomalous center of wave train, i.e., Center 1 near the jet core, thus a positive PNA-like response results (Fig. 11).

Likewise, for the corresponding SE-M3 fields (Fig. 15), strong anomalous upper-level convergence (Fig. 15a) and northerly divergent wind across the jet (Fig. 15b) are induced by the imposed SCS cooling, which then generates the prevailing positive S_L pattern (Fig. 15e) with the aforesaid jet effect. Hence the cyclonic Center 1 is excited due to the supply of positive vorticity, which results in a negative PNA-like response train (Fig. 13). The major anomalous Rossby wave source regions for the two experiments are similar but in opposite fashion, and they locate near the jet core to the north of SCS (Figs. 14e and 15e).

To summarize, relatively strong positive (negative) SCS SSTA arouses upper-level divergence (convergence) and then negative (positive) wave source of unique location, jointly with the Asian jet effect. From such wave source, the positive (negative) PNA-like response is induced.

Note that we have mainly focused on the initial triggering role of SCS SST. The detailed underlying mechanisms, however, are yet to be investigated. For example, it has been realized that the role of transient eddy feedback is especially important in maintaining or strengthening the PNA pattern after excited (e.g., Dai et al. 2017; Guo et al. 2020). Furthermore, it has recently been revealed that, strong transient eddy activity and eddy forcings can accelerate the westerly jet (e.g., Chen et al. 2019; Wang et al. 2019; Chu et al. 2020), by arousing stronger Rossby wave breaking and transient kinetic energy transport (Chen et al. 2019), and such process is associated with the subtropical front zone (STFZ) (e.g., Chen et al. 2020a, b). In this study, the role of the Asian westerly jet is notable, both for the barotropic instability at the jet exit and its vorticity effect as a wave source. That is to say, the transient eddy

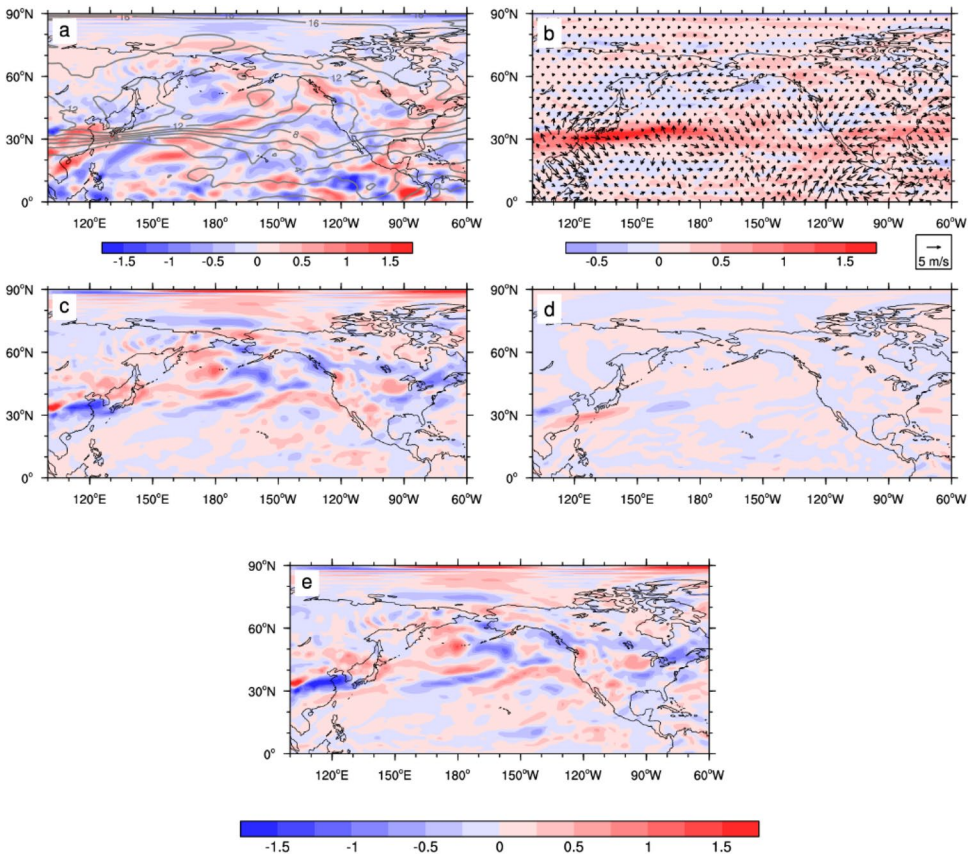

Fig. 14 The 250-hPa anomalous S_L with associated terms for SE-P4 at day − 14, described by the differences with CTL. (a) D_L (shading: interval is 0.25×10^{-5} s^{-1}) and $\left(\overline{\zeta}+f\right)$ (poleward-ascending contours: interval is 2×10^{-5} s^{-1}). (b) The meridional gradient of $\left(\overline{\zeta}+f\right)$ that occupies the major proportion of $\nabla\left(\overline{\zeta}+f\right)$ (shading: interval is 0.25×10^{-10} m^{-1} s^{-1}) and $\mathbf{v}_{\chi L}$ (arrows: scaling is 5 m s^{-1}). The (c) divergence component of S_L: $-\left(\overline{\zeta}+f\right)D_L$, (d) advection component of S_L: $-\boldsymbol{v}_{\chi L}\bullet\nabla\left(\overline{\zeta}+f\right)$, and (e) total S_L: $-\left(\overline{\zeta}+f\right)D_L-\mathbf{v}_{\chi L}\bullet\nabla\left(\overline{\zeta}+f\right)$ are shaded with the interval of 0.25×10^{-9} s^{-2}

may also affect the SCS-induced response by affecting the westerly jet. All these issues are worth a careful examination, and will be investigated using a rigorously developed multiscale energetics analysis (Liang and Anderson 2007; Liang, 2016b).

6 Summary

The Pacific–North American (PNA) teleconnection pattern has long been considered as an extratropical response to ENSO, but in fact ENSO cannot fully explain it. Through causal inference with the newly rigorously developed information flow analysis, this study has revealed a remarkable impact of the South China Sea (SCS) on the growth of PNA. The information flow rate, which measures the strength of causality, from the Pacific SSTA to the PNA index shows a distinctly high center of causality within the SCS, apart from the well-known causality within the ENSO region. The causal pattern within the SCS is quite localized in its interior rather than periphery, indicating that the causality is from the local SST variability within the SCS. It has been shown that the causality is rather robust; it exists with different datasets, and lasts through time.

To verify the newly revealed SCS effect, a set of experiments have been conducted with Community Earth System Model (CESM). Sensitivity experiments have been designed with purported SCS warming and cooling. By comparing the forced PNA evolutions to the standard case, remarkable PNA-like responses have been revealed. Specifically, relatively strong positive (negative) SCS SSTA would arouse positive (negative) propagating PNA-like response, which is led by a precursory anticyclonic (cyclonic) center. Through propagating along the jet waveguide, and through being dispersed at the jet exit, the responded wave train carries energy toward Pacific and North America, and hence affects the PNA growth. To understand the underlying dynamics, the Rossby wave source is diagnosed to locate the wave origin. It shows that positive (negative) SCS SSTA arouses upper-level

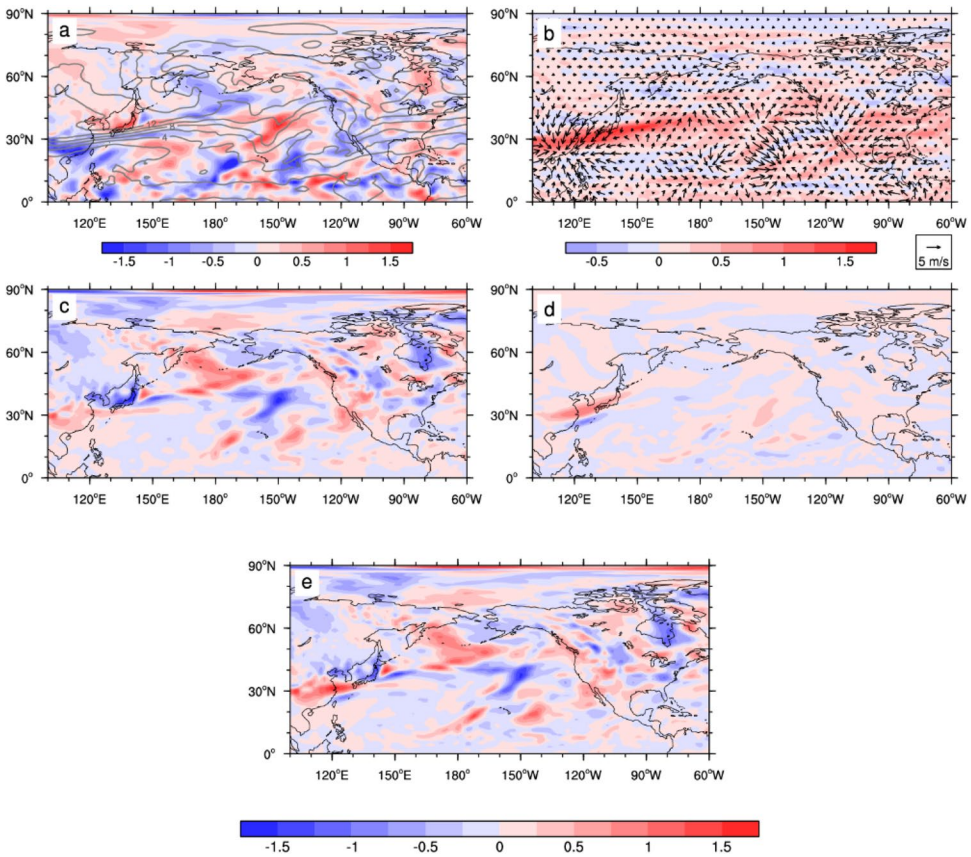

Fig. 15 As in Fig. 14, but for SE-M3

divergence (convergence). Together with the Asian jet effect, this generates a unique negative (positive) wave source near the jet core to the north of SCS. The anticyclonic (cyclonic) center leading to the response train is induced by the negative (positive) wave source. In a word, the SCS indeed serves as a unique forcing that drives PNA.

This study suggests that the SCS effect should be included in interpreting the formation and growth of PNA. It is expected that, by taking the SCS effect into account, a better model can be built for this climate mode toward more accurate predictions.

Acknowledgements Three referees' comments have helped improve the manuscript. We thank NOAA, NCAR, and NCEP for the model and data, and Supercomputing Center of Nanjing University of Information Science and Technology for providing computational resources. This work was supported in part by the National Natural Science Foundation of China under Grant 41975064 and the 2015 Jiangsu Program for Innovation Research and Entrepreneurship Groups.

Funding The funding has been received from National Natural Science Foundation of China with Grant no. 41975064; Jiangsu Program for Innovation Research and Entrepreneurship Groups.

References

Archambault HM, Keyser D, Bosart LF (2010) Relationships between large-scale regime transitions and major cool-season precipitation events in the northeastern United States. Mon Wea Rev 138:3454–3473. https://doi.org/10.1175/2010MWR3362.1

Barnston AG, Livezey RE (1987) Classification, seasonality and persistence of low-frequency atmospheric circulation patterns. Mon Wea Rev 115:1083–1126. https://doi.org/10.1175/1520-0493(1987)115%3c1083:CSAPOL%3e2.0.CO;2

Baxter S, Nigam S (2013) A subseasonal teleconnection analysis: PNA development and its relationship to the NAO. J Clim 26:6733–6741. https://doi.org/10.1175/JCLI-D-12-00426.1

Branstator G (1990) Low-frequency patterns induced by stationary waves. J Atmos Sci 47:629–649. https://doi.org/10.1175/1520-0469(1990)047%3c0629:LFPIBS%3e2.0.CO;2

Branstator G (1992) The maintenance of low-frequency atmospheric anomalies. J Atmos Sci 49:1924–1946. https://doi.org/10.1175/1520-0469(1992)049%3c1924:TMOLFA%3e2.0.CO;2

Branstator G (2014) Long-lived response of the midlatitude circulation and storm tracks to pulses of tropical heating. J Clim 27:8809–8826. https://doi.org/10.1175/JCLI-D-14-00312.1

Cash BA, Lee S (2001) Observed nonmodal growth of the pacific-north American teleconnection pattern. J Clim 14:1017–1028. https://doi.org/10.1175/1520-0442(2001)014%3c1017:ONGOTP%3e2.0.CO;2

Chen Q, Hu H, Ren X, Yang X-Q (2019) Numerical simulation of midlatitude upper-level zonal wind response to the change of north pacific subtropical front strength. J Geophys Res Atmos 124:4891–4912. https://doi.org/10.1029/2018JD029589

Chen F, Chen Q, Hu H et al (2020) Synergistic effects of midlatitude atmospheric upstream disturbances and oceanic subtropical front intensity variability on western pacific jet stream in winter. J Geophys Res Atmos 125:88. https://doi.org/10.1029/2020JD032788

Chen F, Hu H, Bai H (2020b) Subseasonal coupling between subsurface subtropical front and overlying atmosphere in North pacific in winter. Dyn Atmos Oceans 90:101145. https://doi.org/10.1016/j.dynatmoce.2020.101145

Chu C, Hu H, Yang X-Q, Yang D (2020) Midlatitude atmospheric transient eddy feedbacks influenced ENSO-associated wintertime Pacific teleconnection patterns in two PDO phases. Clim Dyn 54:2577–2595. https://doi.org/10.1007/s00382-020-05134-4

Corti S, Palmer TN (1997) Sensitivity analysis of atmospheric low-frequency variability. Quart J R Meteor Soc 123:2425–2447. https://doi.org/10.1002/qj.49712354413

Dai Y, Feldstein SB, Tan B, Lee S (2017) Formation mechanisms of the pacific-north American teleconnection with and without its canonical tropical convection pattern. J Clim 30:3139–3155. https://doi.org/10.1175/JCLI-D-16-0411.1

Drouard M, Rivière G, Arbogast P (2015) The link between the north pacific climate variability and the north atlantic oscillation via downstream propagation of synoptic waves. J Clim 28:3957–3976. https://doi.org/10.1175/JCLI-D-14-00552.1

Feldstein SB (2000) The timescale, power spectra, and climate noise properties of teleconnection patterns. J Clim 13:4430–4440. https://doi.org/10.1175/1520-0442(2000)013%3c4430:TTPSAC%3e2.0.CO;2

Feldstein SB (2002) Fundamental mechanisms of the growth and decay of the PNA teleconnection pattern. Quart J R Meteor Soc 128:775–796. https://doi.org/10.1256/0035900021643683

Franzke C, Feldstein SB, Lee S (2011) Synoptic analysis of the Pacific-North American teleconnection pattern. Quart J R Meteor Soc 137:329–346. https://doi.org/10.1002/qj.768

Gordon AL, Huber BA, Metzger EJ et al (2012) South China sea throughflow impact on the Indonesian throughflow. Geophys Res Lett 39:L11602. https://doi.org/10.1029/2012GL052021

Guo Y, Wen Z, Tan Y, Li X (2020) Plausible causes of the interdecadal change of the North Pacific teleconnection pattern in boreal spring around the late 1990s. Clim Dyn 55:1427–1442. https://doi.org/10.1007/s00382-020-05334-y

Henderson SA, Vimont DJ, Newman M (2020) The critical role of non-normality in partitioning tropical and extratropical contributions to PNA growth. J Clim 33:6273–6295. https://doi.org/10.1175/JCLI-D-19-0555.1

Horel JD, Wallace JM (1981) Planetary-scale atmospheric phenomena associated with the southern oscillation. Mon Wea Rev 109:813–829. https://doi.org/10.1175/1520-0493(1981)109%3c0813:PSAPAW%3e2.0.CO;2

Hoskins BJ, Karoly DJ (1981) The steady linear response of a spherical atmosphere to thermal and orographic forcing. J Atmos Sci 38:1179–1196. https://doi.org/10.1175/1520-0469(1981)038%3c1179:TSLROA%3e2.0.CO;2

Hurrell JW, Hack JJ, Shea D et al (2008) A new sea surface temperature and sea ice boundary dataset for the community atmosphere model. J Clim 21:5145–5153. https://doi.org/10.1175/2008JCLI2292.1

Hurrell JW, Holland MM, Gent PR et al (2013) The community earth system model: a framework for collaborative research. Bull Am Meteor Soc 94:1339–1360. https://doi.org/10.1175/BAMS-D-12-00121.1

Jiang S, Hu H, Zhang N et al (2019) Multi-source forcing effects analysis using Liang-Kleeman information flow method and the community atmosphere model (CAM4.0). Clim Dyn 53:6035–6053. https://doi.org/10.1007/s00382-019-04914-x

Jin F, Hoskins BJ (1995) The direct response to tropical heating in a baroclinic atmosphere. J Atmos Sci 52:307–319. https://doi.org/10.1175/1520-0469(1995)052%3c0307:TDRTTH%3e2.0.CO;2

Lau N-C (1988) Variability of the observed midlatitude storm tracks in relation to low-frequency changes in the circulation pattern. J Atmos Sci 45:2718–2743. https://doi.org/10.1175/1520-0469(1988)045%3c2718:VOTOMS%3e2.0.CO;2

Leathers DJ, Yarnal B, Palecki MA (1991) The Pacific/North American teleconnection pattern and US climate. Part I: regional temperature and precipitation associations. J Clim 4:517–528. https://doi.org/10.1175/1520-0442(1991)004%3c0517:TPATPA%3e2.0.CO;2

Li C, Wettstein JJ (2012) Thermally driven and Eddy–Driven jet variability in reanalysis. J Clim 25:1587–1596. https://doi.org/10.1175/JCLI-D-11-00145.1

Li N, Shang SP, Shang SL, Zhang CY (2007) On the consistency in variations of the South China Sea Warm Pool as revealed by three sea surface temperature datasets. Remote Sens Environ 109:118–125. https://doi.org/10.1016/j.rse.2006.12.012

Li X, Hu Z-Z, Liang P, Zhu J (2019) Contrastive influence of ENSO and PNA on variability and predictability of North American winter precipitation. J Clim 32:6271–6284. https://doi.org/10.1175/JCLI-D-19-0033.1

Lian T, Chen D (2012) An evaluation of rotated EOF analysis and its application to tropical pacific SST variability. J Clim 25:5361–5373. https://doi.org/10.1175/JCLI-D-11-00663.1

Liang XS (2008) Information flow within stochastic dynamical systems. Phys Rev E 78:031113. https://doi.org/10.1103/PhysRevE.78.031113

Liang XS (2014) Unraveling the cause-effect relation between time series. Phys Rev E 90:052150. https://doi.org/10.1103/PhysRevE.90.052150

Liang XS (2016a) Information flow and causality as rigorous notions ab initio. Phys Rev E 94:052201. https://doi.org/10.1103/PhysRevE.94.052201

Liang XS (2016b) Canonical transfer and multiscale energetics for primitive and quasigeostrophic atmospheres. J Atmos Sci 73:4439–4468. https://doi.org/10.1175/JAS-D-16-0131.1

Liang XS (2021) Normalized multivariate time series causality analysis and causal graph reconstruction. Entropy 23:679. https://doi.org/10.3390/e23060679

Liang XS, Anderson DGM (2007) Multiscale window transform. Multisc Model Simul 6:437–467. https://doi.org/10.1137/06066895X

Liang XS, Kleeman R (2005) Information transfer between dynamical system components. Phys Rev Lett 95:244101. https://doi.org/10.1103/PhysRevLett.95.244101

Liang XS, Yang X-Q (2021) A note on causation versus correlation in an extreme situation. Entropy 23:316. https://doi.org/10.3390/e23030316

Liu Q, Wang D, Jiang Y et al (2002) Seasonal variation and formation mechanism of the South China Sea warm water. Acta Oceanol Sin 21:331–343

Luo D, Ge Y, Zhang W, Dai A (2020) A unified nonlinear multiscale interaction model of Pacific-North American teleconnection patterns. J Atmos Sci 77:1387–1414. https://doi.org/10.1175/JAS-D-19-0312.1

Miller AJ, Cayan DR, Barnett TP et al (1994) The 1976–77 climate shift of the Pacific Ocean. Oceanography 7:21–26

Mori M, Watanabe M (2008) The growth and triggering mechanisms of the PNA: a MJO-PNA coherence. J Meteor Soc Jpn 86:213–236. https://doi.org/10.2151/jmsj.86.213

Nan F, Xue H, Yu F (2015) Kuroshio intrusion into the South China Sea: a review. Prog Oceanogr 137:314–333. https://doi.org/10.1016/j.pocean.2014.05.012

Neale RB, Chen C-C, Gettelman A, et al (2010) Description of the NCAR Community Atmosphere Model (CAM5.0). NCAR Tech Note NCAR/TN-486+STR

Oleson W, Lawrence M, Bonan B, et al (2010) Technical Description of version 4.0 of the Community Land Model (CLM). NCAR Tech Note NCAR/TN-478+STR

Palmer TN (1988) Medium and extended range predictability and stability of the Pacific/North American mode. Quart J R Meteor Soc 114:691–713. https://doi.org/10.1002/qj.49711448108

Pinto JG, Reyers M, Ulbrich U (2011) The variable link between PNA and NAO in observations and in multi-century CGCM simulations. Clim Dyn 36:337–354. https://doi.org/10.1007/s00382-010-0770-x

Qu T, Du Y, Sasaki H (2006) South China Sea throughflow: a heat and freshwater conveyor. Geophys Res Lett 33:L23617. https://doi.org/10.1029/2006GL028350

Rayner NA, Parker DE, Horton EB et al (2003) Global analyses of sea surface temperature, sea ice, and night marine air temperature since the late nineteenth century. J Geophys Res Atmos 108:4407. https://doi.org/10.1029/2002JD002670

Renshaw AC, Rowell DP, Folland CK (1998) Wintertime low-frequency weather variability in the north Pacific-American Sector 1949–93. J Clim 11:1073–1093. https://doi.org/10.1175/1520-0442(1998)011%3c1073:WLFWVI%3e2.0.CO;2

Reynolds RW, Smith TM, Liu C et al (2007) Daily high-resolution-blended analyses for sea surface temperature. J Clim 20:5473–5496. https://doi.org/10.1175/2007JCLI1824.1

Riddle EE, Stoner MB, Johnson NC et al (2013) The impact of the MJO on clusters of wintertime circulation anomalies over the North American region. Clim Dyn 40:1749–1766. https://doi.org/10.1007/s00382-012-1493-y

Roxy M, Tanimoto Y (2012) Influence of sea surface temperature on the intraseasonal variability of the South China Sea summer monsoon. Clim Dyn 39:1209–1218. https://doi.org/10.1007/s00382-011-1118-x

Saha S, Moorthi S, Pan H-L et al (2010) The NCEP climate forecast system reanalysis. Bull Am Meteor Soc 91:1015–1058. https://doi.org/10.1175/2010BAMS3001.1

Sardeshmukh PD, Hoskins BJ (1988) The generation of global rotational flow by steady idealized tropical divergence. J Atmos Sci 45:1228–1251. https://doi.org/10.1175/1520-0469(1988)045%3c1228:TGOGRF%3e2.0.CO;2

Seo K-H, Lee H-J (2017) Mechanisms for a PNA-like teleconnection pattern in response to the MJO. J Atmos Sci 74:1767–1781. https://doi.org/10.1175/JAS-D-16-0343.1

Seo K-H, Lee H-J, Frierson DMW (2016) Unraveling the teleconnection mechanisms that induce wintertime temperature anomalies over the northern hemisphere continents in response to the MJO. J Atmos Sci 73:3557–3571. https://doi.org/10.1175/JAS-D-16-0036.1

Shukla J, Wallace JM (1983) Numerical simulation of the atmospheric response to equatorial Pacific Sea surface temperature anomalies. J Atmos Sci 40:1613–1630. https://doi.org/10.1175/1520-0469(1983)040%3c1613:NSOTAR%3e2.0.CO;2

Simmons AJ (1982) The forcing of stationary wave motion by tropical diabatic heating. Quart J R Meteor Soc 108:503–534. https://doi.org/10.1002/qj.49710845703

Simmons AJ, Wallace JM, Branstator GW (1983) Barotropic wave propagation and instability, and atmospheric teleconnection patterns. J Atmos Sci 40:1363–1392. https://doi.org/10.1175/1520-0469(1983)040%3c1363:BWPAIA%3e2.0.CO;2

Song J (2018) Understanding anomalous synoptic eddy vorticity forcing in Pacific-North American teleconnection pattern events. J Atmos Sci 75:4287–4312. https://doi.org/10.1175/JAS-D-18-0071.1

Storto A, Masina S (2016) C-GLORSv5: an improved multipurpose global ocean eddy-permitting physical reanalysis. Earth Syst Sci Data 8:679–696. https://doi.org/10.5194/essd-8-679-2016

Straus DM, Shukla J (2002) Does ENSO force the PNA? J Clim 15:2340–2358. https://doi.org/10.1175/1520-0442(2002)015%3c2340:DEFTP%3e2.0.CO;2

Takaya K, Nakamura H (2001) A formulation of a phase-independent wave-activity flux for stationary and migratory quasigeostrophic eddies on a zonally varying basic flow. J Atmos Sci 58:608–627. https://doi.org/10.1175/1520-0469(2001)058%3c0608:AFOAPI%3e2.0.CO;2

Tao L, Liang XS, Cai L et al (2021) Relative contributions of global warming, AMO and IPO to the land precipitation variabilities since 1930s. Clim Dyn 56:2225–2243. https://doi.org/10.1007/s00382-020-05584-w

Toride K, Hakim GJ (2021) Influence of low-frequency PNA variability on MJO teleconnections to North American atmospheric river activity. Geophys Res Lett 48:94078. https://doi.org/10.1029/2021GL094078

Trenberth KE, Branstator GW, Karoly D et al (1998) Progress during TOGA in understanding and modeling global teleconnections associated with tropical sea surface temperatures. J Geophys Res Oceans 103:14291–14324. https://doi.org/10.1029/97JC01444

Vaid BH, Polito PS (2016) Influence of the South China sea biweekly sea surface temperature on the South China sea summer monsoon especially during the Indian ocean dipole. Atmos Ocean 54:48–59. https://doi.org/10.1080/07055900.2015.1130682

Wallace JM, Gutzler DS (1981) Teleconnections in the geopotential height field during the northern hemisphere winter. Mon Wea Rev 109:784–812. https://doi.org/10.1175/1520-0493(1981)109%3c0784:TITGHF%3e2.0.CO;2

Wang C, Wang W, Wang D, Wang Q (2006) Interannual variability of the South China Sea associated with El Niño. J Geophys Res Oceans 111:C03023. https://doi.org/10.1029/2005JC003333

Wang G, Su J, Ding Y, Chen D (2007) Tropical cyclone genesis over the south China sea. J Mar Syst 68:318–326. https://doi.org/10.1016/j.jmarsys.2006.12.002

Wang L, Hu H, Yang X (2019) The atmospheric responses to the intensity variability of subtropical front in the wintertime North Pacific. Clim Dyn 52:5623–5639. https://doi.org/10.1007/s00382-018-4468-9

Xiao H, Zhang F, Miao L et al (2020) Long-term trends in Arctic surface temperature and potential causality over the last 100 years. Clim Dyn. https://doi.org/10.1007/s00382-020-05330-2

Yang Y, Xie S-P, Du Y, Tokinaga H (2015) Interdecadal difference of interannual variability characteristics of South China sea SSTs associated with ENSO. J Clim 28:7145–7160. https://doi.org/10.1175/JCLI-D-15-0057.1

Yang P, Wang G, Zhang F, Zhou X (2016) Causality of global warming seen from observations: a scale analysis of driving force of the surface air temperature time series in the Northern Hemisphere. Clim Dyn 46:3197–3204. https://doi.org/10.1007/s00382-015-2761-4

Zhang F, Lei Y, Yu Q-R et al (2017a) Causality of the drought in the Southwestern United States based on observations. J Climate 30:4891–4896. https://doi.org/10.1175/JCLI-D-16-0601.1

Zhang F, Yang P, Fraedrich K et al (2017b) Reconstruction of driving forces from nonstationary time series including stationary regions and application to climate change. Physica A 473:337–343. https://doi.org/10.1016/j.physa.2016.12.088

Zhao Y, Liang XS, Gan J (2016) Nonlinear multiscale interactions and internal dynamics underlying a typical eddy-shedding event at Luzon Strait. J Geophys Res Oceans 121:8208–8229. https://doi.org/10.1002/2016JC012483

Zhou F, Ren H-L, Xu X-F, Zhou Y (2017) Understanding positive feedback between PNA and synoptic eddies by eddy structure decomposition method. Clim Dyn 48:3813–3827. https://doi.org/10.1007/s00382-016-3304-3